Available online at www.sciencedirect.com

Chemical Engineering Research and Design

journal homepage: www.elsevier.com/locate/cherd

A theoretical and experimental investigation of batch oil-water gravity separation

*Moein Assar, Sébastien Simon, Geir Humborstad Sørland, Brian Arthur Grimes**

Ugelstad Laboratory, Department of Chemical Engineering, Norwegian University of Science and Technology (NTNU), N-7491 Trondheim, Norway

ARTICLE INFO

Article history:
Received 3 October 2022
Received in revised form 3 April 2023
Accepted 12 April 2023
Available online 14 April 2023

Keywords:
Population balance model
Dense packed layer
Multiphase fluid
Particulate system
Gravity separator

ABSTRACT

Gravity separation of oil-water emulsions is an industrially crucial process. Mechanistic models for a batch separation process can immensely be beneficial by linking emulsion experimental characterization to optimal industrial equipment design. For this reason, a mathematical model for this process was developed, which considers droplets settling/rising due to buoyancy force, binary and interfacial coalescence of the droplets using a film drainage model, and formation of a homophase. Various models for the droplet slip velocity were compared, which exhibit similar predictions using the Kumar and Hartland model and Behzadi et al. model while different from the Zaki and Richardson model. Another crucial part of the model is the proper mathematical description for forming the dense-packed layer (DPL). This study proposes a new approach to improve the prediction for the DPL formation by introducing diffusion in the model as an advection-diffusion equation. Accordingly, a suitable closure model for effective diffusion coefficient was selected, ensuring physical volume fraction range (0–1) in the system. Finally, the proposed closure model was tuned using experimental data for a stabilized water in model oil emulsion. Experiments were performed by the NMR technique for a wide range of initial water volume fractions (20–60%). The model prediction agrees well with the experiments. In particular, simultaneous agreement with all cases having various initial volume fractions and droplet size distributions suggests that this model can be generalized and applied to a wide range of oil and water emulsions. Additionally, the developed model shows promise as it can ensure physical values for volume fractions.

© 2023 The Authors. Published by Elsevier Ltd on behalf of Institution of Chemical Engineers. This is an open access article under the CC BY license (http://creativecommons.org/licenses/by/4.0/).

1. Introduction

The separation of oil-water emulsions under the gravitational effect is widely applied in many industries such as food, chemical, petrochemical, and petroleum (Grimes, 2012). Particularly, gravitational separators are ubiquitous in the crude oil industry due to economic reasons and simplicity (Panjwani et al., 2015). The ever-increasing rate of produced water in the existing oil field and the production from heavier crude oil fields are two main aspects that have made this process even more critical. Commonly, emulsions formed in the petroleum industry can be widely diverse regarding behavior and stability. The mentioned fact is attributed to the high dependency on crude oil and water compositions (Oshinowo et al., 2016).

Reviewing the literature, there exists several experimental techniques to measure the dispersed phase volume fraction profiles for sedimentation and creaming processes. Bury et al. (1995) developed a technique based on conductivity measurements. They converted conductivities into volume

* Corresponding author.
E-mail address: brian.a.grimes@ntnu.no (B.A. Grimes).
https://doi.org/10.1016/j.cherd.2023.04.029
0263-8762/© 2023 The Authors. Published by Elsevier Ltd on behalf of Institution of Chemical Engineers. This is an open access article under the CC BY license (http://creativecommons.org/licenses/by/4.0/).

Nomenclature

A	gravity settler cross sectional area m^2
B	Hamaker constantNm^2
C	model parameter for effective diffusion coefficient m
C_d	drag coefficient
$C_{d,\infty}$	drag coefficient for a single droplet in an infinitely dilute dispersion
D_e	effective diffusion coefficient m^2s^{-1}
$f_{n,r}$	radius-based number density distribution $m^{-3}m^{-1}$
$f_{v,r}$	radius-based volume density distribution m^{-1}
$\hat{f}_{v,r}$	dimensionless radius-based volume density distribution
$f_{v,r,0}$	initial radius-based volume density distribution m^{-1}
$\hat{f}_{v,r,0}$	initial dimensionless radius-based volume density distribution
$f_{n,v}$	volume-based number density distribution $m^{-3}m^{-3}$
F	volume-fraction hindrance effect coefficient
g	gravitational acceleration ms^{-2}
H	gravity settler height m
H_i	dispersion phase height m
$\hat{H}_i$	dimensionless dispersion phase height
k_B	Boltzmann constant JK^{-1}
k_c	binary coalescence rate m^3s^{-1}
$\hat{k}_c$	dimensionless binary coalescence rate
k_{CE}	empirical tuning parameter for the binary coalescence efficiency
k_{CR}	empirical tuning parameter for the collision rate
k_{IC}	empirical tuning parameter for the interfacial coalescence time
m	model parameter for effective diffusion coefficient
n	model parameter for effective diffusion coefficient
n_{ic}	interfacial convective flux s^{-1}
Pe	droplet Peclet number
Pe_{bc}	droplet pair Peclet number used for binary coalescence
Q_d	volumetric flow rate of the dispersed phase across the interface m^3s^{-1}
r	droplet radius m
$\hat{r}$	dimensionless droplet radius
r_m	largest droplet radius considered for numerical analysis m
$R_{b,n,r}$	coalescence birth rate for radius-based number density $m^{-3}m^{-1}s^{-1}$
$R_{b,n,v}$	coalescence birth rate for volume-based number density $m^{-3}m^{-3}s^{-1}$
$R_{b,v,r}$	coalescence birth rate for radius-based volume density $m^{-1}s^{-1}$
$\hat{R}_{b,v,r}$	dimensionless coalescence birth rate for radius-based volume density
$R_{d,n,r}$	coalescence death rate for radius-based number density $m^{-3}m^{-1}s^{-1}$
$R_{d,n,v}$	coalescence death rate for volume-based number density $m^{-3}m^{-3}s^{-1}$
$R_{d,v,r}$	coalescence death rate for radius-based volume density $m^{-1}s^{-1}$
$\hat{R}_{d,v,r}$	dimensionless coalescence death rate for radius-based volume density
Re	droplet Reynolds number
t	time s
$\hat{t}$	dimensionless time
t_{bc}	binary film drainage and rupture (coalescence) time s
t_{ic}	interfacial film drainage and rupture (coalescence) time s
T	absolute temperature K
u_c	continuous phase velocity ms^{-1}
u_d	dispersed phases settling/rising velocity ms^{-1}
$\hat{u}_d$	dispersed phases dimensionless settling/rising velocity
u_{ic}	equivalent droplet interfacial velocity for a coalescing droplet ms^{-1}
$\hat{u}_{ic}$	equivalent dimensionless droplet interfacial velocity for a coalescing droplet
u_s	slip velocity between continuous and dispersed phases ms^{-1}
u_0	characteristic velocity ms^{-1}
v	droplet volume m^3
v_m	largest droplet volume considered for numerical analysis m^3
V_h	volume of the separated phase m^3
z	spatial coordinate variable m
$\hat{z}$	dimensionless spatial coordinate variable
γ	interfacial tension Nm^{-1}
μ_c	continuous phase viscosity $Nm^{-2}s$
μ_r	average droplet radius m
$\hat{\mu}_r$	dimensionless average droplet radius
ρ_c	continuous phase density kgm^{-3}
ρ_d	dispersed phase density kgm^{-3}
ϕ_d	disperse phase volume fraction
ϕ_m	maximum dispersed phase volume fraction (model parameter for effective diffusion coefficient)
ψ_c	binary droplet coalescence efficiency
ω_c	binary droplet collision rate m^3s^{-1}

fraction values of the dispersed phase in terms of dispersion dielectric theory and showed that the conductivity method is sensitive to small changes in the volume fraction of dispersed phase observed at room temperature. Another powerful technique is based on ultrasonic spectrometry, where the frequency dependence of the ultrasonic attenuation coefficient is measured for an emulsion followed by interpreting the resulting spectra via an ultrasonic scattering theory (Chanamai et al., 1999). Abeynaike et al. (2012) used an optical technique taking advantage of optical contrast between the biodiesel and glycerol and studied sedimentation / creaming of dispersions. Deb et al. (2022) compared two techniques, namely turbidimetry and Raman Spectroscopy, for monitoring a creaming process. They stated that turbidimetry is able to accurately measure the dispersed phase volume fraction off-line while Raman spectroscopy has the potential for in situ monitoring of a creaming system.

Another possible way to characterize emulsions is via a batch gravity separation experiment and monitor the experiments employing the low field nuclear magnetic resonance technique (LF NMR) (Sjöblom et al., 2021). Thereby,

one can quantify various parameters like droplet size distribution (DSD) and dispersed phase volume fraction profiles at different times and in a non-intrusive manner. Here, a predictive model derived from the first principles can help correlate the experimental observations in terms of separation behavior to fundamental understanding about the binary or interfacial coalescence as well as the polydisperse settling/rising of the droplets in the system. In other words, these models allow the characterization of colloidal systems for specific cases through tuning the model parameters. Subsequently, these tuned models can be utilized in the optimal design of oil-water separation equipment.

The batch gravity separation of oil-water dispersions (including creaming and sedimentation processes based on the continuous and dispersed phases) can generally be governed by several mechanisms. Buoyancy-driven transport results in spatial and temporal variations in the density distribution of dispersed droplets. At the same time, pairs of droplets can collide and coalesce, resulting in larger droplets that can sediment/cream faster. A homophase can also be formed (top of column for creaming and bottom for sedimentation). Droplets reaching the liquid-liquid interface can coalesce and integrate with the homophase resulting in its growth and the contraction of the dispersion layer. The rate at which this coalescence takes place can determine the existence of a dense-packed layer (DPL), a packed bed of dispersed phase droplets with a high volume fraction (Panjwani et al., 2015). This layer is formed if the overall rate of interfacial coalescence is lower than that of sedimentation. In this layer, the volume fraction can be extensively increased due to polydispersity and the droplet's tendency to deform under the squeezing force exerted by the weight of the overhead droplets.

Despite the apparent simplicity of the gravity separation process, a fully accommodating model is not available mainly because of the various assumptions and levels of complexity involved in building such models described as follows. Despite these variations, population balance modeling is an indispensable part of such models to consider polydispersity in the system. Wang and Davis (1995) considered simultaneous sedimentation and coalescence according to differential sedimentation of droplets. The assumption of dilute dispersion allowed them to neglect the volume fraction hindrance effect for the settling velocity. They also assumed no resistance to interfacial coalescence. Their model tracks the liquid-liquid interface explicitly via an overall mass balance. Concurrently, the shrinking dispersion layer is implicitly accounted for in their model. Cunha et al. (2008) developed their population balance model according to stokes settling velocity and binary coalescence based on simultaneous differential sedimentation and Brownian motion. They assumed an interfacial coalescence velocity proportional to the height of the dense-packed layer and independent of the droplet size. This was to account for the compression force exerted by the weight of the DPL. They incorporated three tuning parameters for sedimentation velocity as well as binary and interfacial coalescence rates to fit the model to their crude oil-water experiments. In their model, they considered a diffusive term; however, they did not report any function form, numerical value, or physical justification for this term. Their model also lacks consideration for the homophase's growth and contraction of the dispersion layer. Grimes (2012) developed his model according to hindered settling velocity model proposed by Richardson and Zaki (1954) and simultaneous binary and interfacial coalescence according to a film drainage model. He used a temporal-spatial transformation to tackle the moving boundary problem that emerged due to the homophase growth. In a second paper (Grimes et al., 2012), he validated the model versus experimental data. There are more recent attempts to further improve the model. (Antonio García and Fernando Betancourt, 2019) developed their model by adopting different coalescence rates. For the sedimentation zone, they adopted the coalescence model by Rogers and Davis (1990), which is based on differential sedimentation force between droplets. For the DPL, they used the rate proposed by Ruiz and Padilla (1996), which accounts for both droplet size and the compression force from the weight of the DPL. They employed the Kumar and Hartland equation (Kumar and Hartland, 1985) for the droplet slip velocity, which considers both the volume fraction hindrance effect and the non-stokes flow regimes. Additionally, their model contains a correction procedure by turning off the coalescence birth term in case of unphysical values for the volume fractions higher than unity. In their later attempt, they also extended this model to a continuous separator (Antonio García et al., 2022).

The major pitfall with the available modeling approach is the inability of the models to adequately describe the formation and growth of the DPL. This shortcoming originally stems from the oversimplification concerning the droplet velocities. In this modeling approach, an empirical terminal velocity model for the droplets is usually used instead of directly solving the continuity and momentum equations for continuous and dispersed phases. This simplification can result in unphysical volume fraction predictions, even outside the physical bound of 0–1. As described, various modeling and numerical strategies were adopted by different researchers to address this challenge. Another approach in the modeling is combining the population balance equation and CFD (PBE-CFD) using available CFD software packages. This will allow the simultaneous solution of the continuity and motion equations for a polydispersed system. Panjwani et al. (2015) used this approach to study the formation of the DPL for a continuous separator. They mentioned in their study that direct modeling of the DPL can be practically restrictive due to the immense span of time and length scales associated with different underlying physics. Oshinowo et al. (2016), in their PBE-CFD model for batch separation, used a multi-fluid Eulerian multiphase approach. They compared their model results versus experimental data obtained by the ultrasonic technique. In their later work (Oshinowo and Vilagines, 2020), they extended their model to simulate a 3-phase separator. From the studied literature, the main challenges with the CFD-PBE approach are the inadequacy of the prediction for the DPL and, at the same time, complexity and expensive computation, which can limit its application for ordinary engineering tasks such as model tuning, and optimization.

In the current study, we aim to improve and extend the previous model by Grimes (2012). The focus of this work would be primarily on improving the prediction for the DPL formation. The main motivation for the current modeling effort is the early works done by Shih et al. (1987, 1986) where they showed that a one-dimensional hydrodynamic model for the sedimentation of the fine particles could be simplified in the form of a diffusion-type equation. In the current work, we propose an advection-diffusion model for batch

sedimentation of oil-water emulsion with a suitable closure model for effective diffusion coefficient. The parameters for this closure model are estimated according to the experiments performed by the LF NMR technique for batch sedimentation of a stabilized model oil. It is worth mentioning that the coalescence models are presented in this work only to keep the generality of the model and these phenomena will be experimentally studied in future works.

2. Mathematical analysis

Theoretically, the gravity separation process for an oil-water dispersion consists of hindered settling/rising of the droplets as well as coalescence of the droplets. Eventually, as the droplets reach the oil-water interface, a homophase can be created and grow due to the interfacial coalescence. The latter phenomenon gives rise to a water phase formation on the bottom for a sedimentation system or an oil phase formation on the top for a creaming system. Suppose the rate of sedimentation is higher than the rate of interfacial coalescence. In that case, one can expect the formation of a DPL on top/bottom of the liquid-liquid interface that initially grows in thickness as more droplets move toward the interface; eventually, this layer can start to shrink as the droplets coalesce into the homophase.

2.1. Dispersion layer model

We consider an initially uniform coalescing dispersion that is under the influence of gravity. Here, the presented model is general and applicable to sedimentation and creaming systems. The only difference is the coordinate origin and the axis direction, which should be along with the settling or rising movement, as depicted in Fig. 1. For a sedimentation system, the origin of the coordinate system is at the top, and the z-axis extends from top to bottom in the direction of droplet sedimentation. For a creaming system, the origin is at the bottom, and the positive z-direction is selected from the bottom to the top.

The mass balance equation for the dispersed phase by considering the advection and diffusion terms takes the following form:

$$\frac{\partial f_{n,r}(r,z,t)}{\partial t} = -\frac{\partial}{\partial z}[u_d(r,z,t)f_{n,r}(r,z,t)] + \frac{\partial}{\partial z}\left(D_e(r,z,t)\frac{\partial f_{n,r}(r,z,t)}{\partial z}\right) + R_{b,n,r} - R_{d,n,r} \quad (1)$$

where $f_{n,r}$ is the radius-based number density distribution for a specific droplet size at a particular column location and time. u_d is the pertinent droplet rising/settling velocity. D_e is the effective diffusion coefficient. $R_{b,n,r}$ and $R_{d,n,r}$ are radius-based birth and death rates consistent with the number density distribution resulting from the binary droplet coalescence, respectively. r, z, t are droplet radius, vertical location in the separation column, and elapsed time from the start of the process, respectively. It must be noted that the diffusion term is added to the model to consider the effect of compressive stress in the DPL based on the insight from the work of Shih et al. (1987, 1986). This matter will be further expanded and discussed in Section 2.4. The radius-based coalescence birth and death rates in Eq. (1) are as follows:

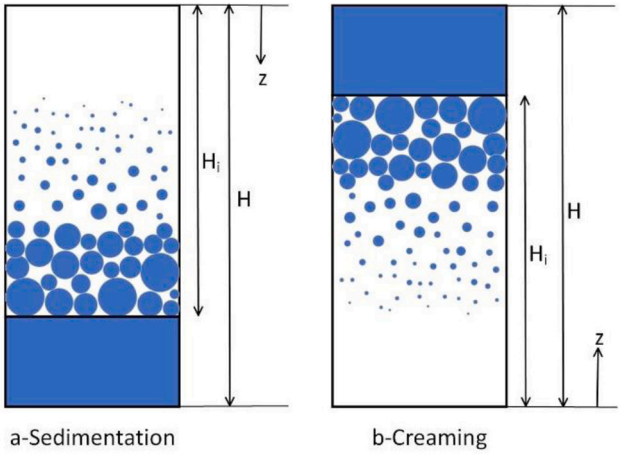

Fig. 1 – Schematic of batch gravity separator, a-sedimentation, b-creaming.

$$R_{b,n,r} = \int_0^{r/\sqrt[3]{2}} k_c(r', r'', z, t) f_{n,r}(r', z, t) f_{n,r}(r'', z, t) \frac{r^2}{r''^2} dr' \quad (2)$$

$$R_{d,n,r} = f_{n,r}(r,z,t) \int_0^{\infty} k_c(r', r'', z, t) f_{n,r}(r', z, t)\, dr' \quad (3)$$

where k_c is the coalescence rate between droplets of sizes v and v'. The interested reader can also refer to the supplementary material for more details about the derivation of this form of PBE. Now, we take another step and change the dependent variable from the number density distribution to the volume density distribution. It is worth noting that in the latter definition, the dependent variable has a more limited range of numerical values. As a result, one can expect lower round-off error issues in the numerical analysis of the problem. Also, the visualization of the results is strengthened. The Volume density distribution is simply defined as below:

$$f_{v,r}(r,z,t) = f_{n,r}(r,z,t) \times \frac{4\pi}{3} r^3 \quad (4)$$

With the above transformation, the governing equation takes the following form.

$$\frac{\partial f_{v,r}(r,z,t)}{\partial t} = -\frac{\partial}{\partial z}[u_d(r,z,t)f_{v,r}(r,z,t)] + \frac{\partial}{\partial z}\left(D_e(r,z,t)\frac{\partial f_{v,r}(r,z,t)}{\partial z}\right) + R_{b,v,r} - R_{d,v,r} \quad (5)$$

$$R_{b,v,r} = \left(\frac{3}{4\pi}\right) r^3 \int_0^{\frac{r}{\sqrt[3]{2}}} \frac{k_c(r', r'', z, t) f_{v,r}(r', z, t) f_{v,r}(r'', z, t)}{r'^3(r^3 - r'^3)} \frac{r^2}{r''^2} dr' \quad (6)$$

$$R_{d,v,r} = \left(\frac{3}{4\pi}\right) f_{v,r}(r,z,t) \int_0^{\infty} k_c(r', r'', z, t) \frac{f_{v,r}(r', z, t)}{r'^3} dr' \quad (7)$$

Following the mentioned definition, the volume fraction and average droplet size can be calculated now utilizing the below integrals:

$$\phi_d(z,t) = \int_0^{\infty} f_{v,r}(r,z,t)\, dr \quad (8)$$

$$\mu_r(z,t) = \frac{1}{\phi_d(z,t)} \int_0^{\infty} r f_{v,r}(r,z,t)\, dr \quad (9)$$

where ϕ_d and μ_r are dispersed phase volume fraction and average droplet radius, respectively.

In the derived model, the droplet size coordinate expands from zero to infinity. Thus, the coordinate should be truncated at a suitable value (r_m) to promote the numerical analysis of the problem. The choice of the mentioned value is critical for generating valid numerical results. A feasible approach for properly selecting the truncation point for the internal coordinate is developed and used to choose this value conservatively for both coalescing and non-coalescing systems in the supplementary material. The above advection-diffusion equation is subject to the below boundary conditions:

- At z = 0 (top or bottom), overall flux is equal to zero
- At z = H_i (interface), overall flux should be calculated according to the interfacial coalescence

The above boundary conditions ensure that the model is thoroughly conservative. These boundary conditions can be mathematically expressed as:

$$u_d(r, z, t)f_{v,r}(r, z, t) - D_e(r, z, t)\frac{\partial f_{v,r}(r, z, t)}{\partial z} = 0 \; at \; z = 0, \; \forall\, t|_{0 < t \le \infty} \; \& \; r|_{0 \le r \le \infty} \tag{10}$$

$$u_d(r, z, t)f_{v,r}(r, z, t) - D_e(r, z, t)\frac{\partial f_{v,r}(r, z, t)}{\partial z} = u_{ic}(r, t)f_{v,r}(r, z, t) \; at \; z = H_i, \; \forall\, t|_{0 < t \le \infty} \; \& \; r|_{0 \le r \le \infty} \tag{11}$$

where u_{ic} is the velocity at which the droplet leaves the dispersed phase by coalescing into the homophase and will be further expanded in Section 2.2. The initial condition for an initially uniform system is as below:

$$f_{v,r}(r, z, t) = f_{v,r,0}(r) \; at \; t = 0, \; \forall\, z|_{0 < z < H_i} \; \& \; r|_{0 \le r \le \infty} \tag{12}$$

2.2. Moving interface model

As described previously, as the dispersed phase gets separated, a new homophase is formed at the bottom/top of the batch separator column. The convective flux for a specific droplet size at the interface can be written as below:

$$n_{ic}(r, H_i, t) = u_{ic}(r, t)f_{v,r}(r, H_i, t) \tag{13}$$

where u_{ic} is the velocity at which the droplet leaves the dispersed phase by coalescing into the homophase. This velocity can be calculated as below:

$$u_{ic}(r, t) = \frac{4r}{3t_{ic}(r, t)} \tag{14}$$

The interested reader can refer to the supplementary material section for details regarding the derivation of Eq. (14). Here, t_{ic} is the interfacial coalescence time for a droplet of size r from getting in contact with the dispersion-homophase interface until fully integrated with the homophase. This term will be further expanded using a parallel film drainage model in Section 2.5. Now, using the following term (Eq. (14)), the total volumetric flow rate of the dispersed phase over the interface can be calculated as:

$$Q_d = A\int_0^\infty u_{ic}(r, t)f_{v,r}(r, H_i, t)\,dr \tag{15}$$

where A is the cross-section of the column. Now, this term can be exploited to calculate the dynamic change in the location of the interface. For that, one can equate the volume change rate for the homophase with this term as below.

$$\frac{dV_h(t)}{dt} = Q_d \tag{16}$$

where V_h is the total volume of the separated homophase and can be written as:

$$V_h = A(H - H_i) \tag{17}$$

By substitution, the final equation for the dynamic change in the interface location yields as:

$$\frac{dH_i(t)}{dt} = -\int_0^\infty u_{ic}(r, t)f_{v,r}(r, H_i, t)\,dr \tag{18}$$

The initial condition for Eq. (18) can be written as below.

$$H_i(t) = H \; at \; t = 0 \tag{19}$$

2.3. Droplet rising/settling velocity

Droplets settle or rise according to the buoyancy force for a dispersion system under the influence of gravity. Bearing that the colloidal droplets move slowly, practically, it is a safe assumption to ignore the inertia terms in the momentum equation (Shih et al., 1986). Based on this assumption, the velocity difference between the continuous and dispersed phases ($u_d - u_c$) becomes equal to the slip velocity, which has the functionality of the droplet size as well as dispersed phase volume fraction as below:

$$u_d(r, z, t) - u_c(z, t) = u_s(r, \phi_d) \tag{20}$$

Simultaneously, while droplets are moving, the volumetric change should be replaced by the continuous phase. The continuity equation expresses this matter as below:

$$(1 - \phi_d)u_c(z, t) + \int_0^\infty f_{v,r}(r, z, t)u_d(r, z, t)\,dr = 0 \tag{21}$$

Slip velocity can be further formulated by considering buoyancy, weight, and drag forces as:

$$u_s(r, \phi_d) = \sqrt{\frac{8gr}{3C_d}\frac{|\rho_d - \rho_c|}{\rho_c}} \tag{22}$$

where g is the gravitational acceleration, ρ_c and ρ_d are continuous and dispersed phase densities, and C_d is the drag coefficient. Behzadi et al. (2004) defined the drag coefficient as the product of the drag coefficient for a single droplet/bubble in an infinitely dilute dispersion ($C_{d,\infty}$) and the volume hindrance effect coefficient (F).

$$C_d(r, \phi_d) = C_{d,\infty}(r)F(\phi_d) \tag{23}$$

They proposed an empirical correlation for the latter functionality for both droplets and bubbles for a wide range of volume fractions (up to 75%). Accordingly, they proposed the following equation for this coefficient:

$$F(\phi_d) = \exp(3.64\phi_d) + \phi_d^{0.864} \tag{24}$$

Alternatively, the hindrance effect coefficient can be calculated based on the equation by Richardson and Zaki (1954) as below:

$$F(\phi_d) = \frac{1}{(1 - \phi_d)^n} \tag{25}$$

The drag coefficient for a single droplet in an infinitely dilute dispersion ($C_{d,\infty}$) can be calculated using the well-known Schiller–Naumann correlation (Shiller and Naumann, 1935) which applies to Reynolds numbers less than 1000.

$$C_{d,\infty}(r) = \frac{24}{\mathrm{Re}(r)}(1 + 0.15\,\mathrm{Re}(r)^{0.687}) \tag{26}$$

Here, the Reynolds number is defined as:

$$\mathrm{Re}(r) = \frac{2\rho_c u_s r}{\mu_c} \tag{27}$$

where μ_c is the continuous phase dynamic viscosity. It is worth noting that in case of the creeping flow regime ($\mathrm{Re} \ll 1$), the slip velocity can be explicitly expressed by the stokes terminal velocity as below:

$$u_s(r, \phi_d) = \frac{2gr^2}{9\mu_c F(\phi_d)} |\rho_d - \rho_c| \tag{28}$$

Another useful empirical equation to calculate the slip velocity is proposed by Kumar and Hartland (1985). It is particularly advantageous as it is valid over a wide range of volume fractions and Reynolds numbers ($\phi_d = 0.01 - 0.76$ and $\mathrm{Re} = 0.16 - 3169$).

$$0.53{u_s}^2 + \frac{12\mu_c}{r\rho_c}u_s + \frac{2rg(\rho_c - \rho_d)(1 - \phi_d)}{3\rho_c(1 + 4.56{\phi_d}^{0.73})} = 0 \tag{29}$$

The slip velocity can be directly calculated by solving the above quadratic polynomial. Now having the slip velocity's numerical value, one can use the momentum and continuity equation (Eqs. (20) and (21)) to calculate the continuous and all the dispersed phase droplets' velocities. Zimmels (1983) has proposed a numerical approach for the mentioned problem. However, this model could not describe our experimental observations, specifically the sharp sedimentation fronts formed during the sedimentation. Thus, we adopted another approach in which the movement effect of the continuous phase in the opposite direction is compensated by multiplying the slip velocity by the continuous phase volume fraction to yield the dispersed phase droplet velocity. According to this assumption, the system is treated similar to a monodispersed system.

$$u_d(r, z, t) = (1 - \phi_d(z, t))u_s(r, \phi_d) \tag{30}$$

2.4. Effective diffusion

Shih et al. (1987, 1986) showed that hyperbolic governing equations for a one-dimensional sedimentation system could be transformed into a diffusion-type equation by ignoring the acceleration terms (owing to the low velocity of the droplets). This approach offers a more straightforward numerical treatment for the governing equations. According to this insight, we added a diffusive term to the governing equation for the dispersion phase. In this section, we propose a closure model for this effective diffusion coefficient initially introduced into the equation. This effective diffusion coefficient is basically the ratio of elasticity to a drag term in the packed region (Shih et al., 1986). For the DPL, elasticity is determined by the compressive stress modulus which has a strong functionality of the volume fraction (Shih et al., 1986). The drag term has the functionalities of physicochemical properties like phase density difference, droplet velocity, as well as volume fraction. The other phenomenon that needs to be addressed by this closure model is the maximum volume fraction in the DPL due to the physical restriction. Rather than selecting one for this value, we introduce the maximum volume fraction allowed in the system (ϕ_m) similar to other researchers work on the emulsion viscosity (Ishii and Zuber, 1979; Krieger and Dougherty, 1959; Mills, 1985). The mentioned parameter allows better tuning according to the experimental data. For a monodispersed system with rigid spheres, packing is $\pi/6 = 0.5236$ (Antonio García and Fernando Betancourt, 2019); however, as a consequence of droplet deformation and polydispersity in liquid-liquid dispersion systems, this value can be higher (typically 0.7–0.9). Additionally, the closure model should satisfy the below two constraints:

- Zero effective diffusion at zero volume fraction
- Infinite effective diffusion at maximum volume fraction

The first constraint is deducted from the fact that in infinitely dilute dispersions, the compressive stress modules and thus the effective diffusion coefficient is zero. The latter constraint is vital as the physical restriction due to high volume fraction can be mathematically described by infinite diffusion. Under these circumstances, all excess droplets at a region with a volume fraction close to ϕ_m will immediately diffuse back to the surrounding regions with a lower volume fraction. This way, the balance equation is forced to conserve the volume fraction between 0-ϕ_m since the effective diffusion goes asymptotically toward infinity as the volume fraction approaches the maximum volume fraction in the system.

In this study, we consider the droplet velocity and volume fraction functionalities as the main parameters for this effective diffusion coefficient. The following function meets the constraints described above, provided that the exponent n and m are positive.

$$D_e(r, z, t) = Cu_d(r, \phi_d)\left(\frac{(\phi_d(z, t)/\phi_m)^n}{(1 - \phi_d(z, t)/\phi_m)^m}\right) \tag{31}$$

where C is the model constant for a specific system and has the dimension of length. n and m are dimensionless exponents for the model. It is worth mentioning that droplet velocity appeared in the equation by assuming that the Stokes flow regime prevails in the DPL.

2.5. Coalescence model

Similar to the work of Grimes (2012), a parallel film drainage model is utilized in the current work. Here, only the equations for the coalescence rates are presented, and the interested reader is referred to mentioned paper for more details about underlying assumptions and derivations. Accordingly, the binary coalescence rate is defined as the product of collision frequency (ω_c) and coalescence efficiency (ψ_c).

$$k_c(r, r', z, t) = \omega_c(r, r', z, t)\psi_c(r, r', z, t) \tag{32}$$

The radius-based equation for collision frequency takes the following form.

$$\omega_c(r, r', z, t) = k_{CR}\frac{k_B T}{6\mu_c}\frac{(r + r')^2}{rr'}[1 + Pe_{bc}(r, r', z, t) + 4.496 (Pe_{bc}(r, r', z, t))^{1/3}] \tag{33}$$

where k_B is the Boltzmann constant, T is absolute temperature, and k_{CR} is the model tuning parameter. Droplet pair Peclet number (Pe_{bc}) is defined as below:

$$Pe_{bc}(r, r', z, t) = \frac{4\pi}{3}\frac{(\rho_d - \rho_c)g}{k_B T}F(\phi_d)rr'|r^2 - r'^2| \tag{34}$$

The radius-based coalescence efficiency can be calculated using the following equation.

$$\psi_c(r, r', z, t) = \exp\left(-\frac{1}{k_{CE}} t_{bc}(r, r', z, t)\right) \tag{35}$$

where k_{CE} is the model tuning parameter and t_{bc} is the binary coalescence time expressed by the following equation.

$$t_{bc}(r, r', z, t) = 1.046 \frac{\mu_c(\rho_d - \rho_c)g}{\gamma^{\frac{3}{2}} B^{\frac{1}{2}}} \left[\frac{rr'}{r + r'}\right]^{9/2} \tag{36}$$

where γ is interfacial tension and B is the Hamaker constant.

According to Eq. (14), the interfacial coalescence time function (t_{ic}) can be determined using the following formula to calculate the interfacial coalescence velocity.

$$t_{ic}(r, z, t) = \frac{1.046}{k_{IC}} \frac{\mu_c(\rho_d - \rho_c)g}{\gamma^{\frac{3}{2}} B^{\frac{1}{2}}} r^{9/2} \tag{37}$$

where k_{IC} is the model tuning parameter. In the presented model, only the buoyancy force is included as the squeezing force to calculate the coalescence efficiency. However, it is still possible to derive similar coalescence rates by considering the compressive force in the DPL. Nevertheless, it is not the focus of the current work and will be considered in a future work.

2.6. *Dimensionless formulation and treating the moving boundary*

The dimensionless form of the governing equations is adopted to analyze the problem numerically. This dimensionless formulation allows immobilization of the moving boundary at the interface, which can be computed on a fixed numerical grid. Thus, all the variables are made dimensionless through the characteristic scales using the following definitions: characteristic length scale as the height of the column (H), characteristic droplet size scale as the maximum droplet size in which the internal domain is truncated (v_m, r_m), the characteristic time scale is calculated by dividing the height of column (H) by a characteristic velocity (u_0) which is the stokes velocity for an initial average droplet size. Using the mentioned scales, all the independent variables can be made dimensionless as follows.

$$\hat{t} = \frac{u_0}{H} t \tag{38}$$

$$\hat{z} = \frac{z}{H_i(t)} = \frac{z}{H\hat{H}_i} \tag{39}$$

$$\hat{r} = \frac{r}{r_m} \tag{40}$$

The dependent variables are made dimensionless using the below definitions.

$$\hat{H}_i(\hat{t}) = \frac{H_i(t)}{H} \tag{41}$$

$$\hat{f}_{v,r}(\hat{r}, \hat{z}, \hat{t}) = f_{v,r}(r, z, t) r_m \tag{42}$$

$$\hat{u}_d(\hat{r}, \hat{z}, \hat{t}) = \frac{u_d(r, z, t)}{u_0} \tag{43}$$

$$Pe(\hat{r}, \hat{z}, \hat{t}) = \frac{u_0 H}{D_e(r, z, t)} \tag{44}$$

$$\hat{k}_c(\hat{r}', \hat{r}'', \hat{z}, \hat{t}) = \frac{H k_c(r', r'', z, t)}{u_0 v_m} \tag{45}$$

$$\hat{u}_{ic}(\hat{r}, \hat{t}) = \frac{u_{ic}(r, t)}{u_0} \tag{46}$$

It must be noted that the new dimensionless independent variable $\hat{z}$ now has the dependency of both time t and spatial coordinate z. As a result, the time derivative $\partial/\partial t$ should be written as a directional derivative in the new dimensionless frame of reference (Grimes, 2012); therefore, it reads as:

$$\frac{\partial f_{v,r}}{\partial t} = \left(\frac{\partial \hat{t}}{\partial t}\right)\left(\frac{\partial \hat{f}_{v,r}}{\partial \hat{t}}\right)\left(\frac{\partial f_{v,r}}{\partial \hat{f}_{v,r}}\right) + \left(\frac{\partial \hat{z}}{\partial t}\right)\left(\frac{\partial \hat{f}_{v,r}}{\partial \hat{z}}\right)\left(\frac{\partial f_{v,r}}{\partial \hat{f}_{v,r}}\right) \tag{47}$$

The partial derivatives in Eq. (47) can be expanded further using the chain rule of differentiation. By doing that and further simplifications, the following equation is obtained.

$$\frac{\partial f_{v,r}}{\partial t} = \left(\frac{u_0}{r_m H}\right)\frac{\partial \hat{f}_{v,r}}{\partial \hat{t}} - \left(\frac{u_0}{r_m H}\right)\left(\frac{\hat{z}}{\hat{H}_i}\right)\left(\frac{\partial \hat{H}_i}{\partial \hat{t}}\right)\frac{\partial \hat{f}_{v,r}}{\partial \hat{z}} \tag{48}$$

Similarly, the convective and diffusive terms can be obtained in the new spatially curvilinear coordinate using the chain rule of differentiation as:

$$\frac{\partial}{\partial z}(u_d f_{v,r}) = \left(\frac{u_0}{r_m H \hat{H}_i}\right)\frac{\partial}{\partial \hat{z}}(\hat{u}_d \hat{f}_{v,r}) \tag{49}$$

$$\frac{\partial f_{v,r}}{\partial z} = \left(\frac{1}{r_m H \hat{H}_i}\right)\frac{\partial \hat{f}_{v,r}}{\partial \hat{z}} \tag{50}$$

$$\frac{\partial}{\partial z}\left(D\frac{\partial f_{v,r}}{\partial z}\right) = \left(\frac{u_0}{r_m H \hat{H}_i^2}\right)\frac{\partial}{\partial \hat{z}}\left(\frac{1}{Pe}\frac{\partial \hat{f}_{v,r}}{\partial \hat{z}}\right) \tag{51}$$

The described approach immobilizes the moving boundary, thereby making the z-coordinate (0-$H_i(t)$) into the new dimensionless coordinate (0–1). Consequently, the equation can now be more conveniently treated numerically as the numerical grid for the spatial dimension is now fixed relative to the position of the interface, H_i. The final equation can be obtained by substituting the derived terms into Eq. (5) as:

$$\begin{aligned}\frac{\partial \hat{f}_{v,r}(\hat{r}, \hat{z}, \hat{t})}{\partial \hat{t}} = {} & \left(\frac{\hat{z}}{\hat{H}_i(\hat{t})}\right)\left(\frac{\partial \hat{H}_i(\hat{t})}{\partial \hat{t}}\right)\frac{\partial \hat{f}_{v,r}(\hat{r}, \hat{z}, \hat{t})}{\partial \hat{z}} \\ & - \left(\frac{1}{\hat{H}_i(\hat{t})}\right)\frac{\partial}{\partial \hat{z}}(\hat{u}_d(\hat{r}, \hat{z}, \hat{t})\hat{f}_{v,r}(\hat{r}, \hat{z}, \hat{t})) + \left(\frac{1}{\hat{H}_i^2(\hat{t})}\right)\frac{\partial}{\partial \hat{z}} \\ & \left(\frac{1}{Pe(\hat{r}, \hat{z}, \hat{t})}\frac{\partial \hat{f}_{v,r}(\hat{r}, \hat{z}, \hat{t})}{\partial \hat{z}}\right) + \hat{R}_{b,v,r} - \hat{R}_{d,v,r}\end{aligned} \tag{52}$$

where dimensionless birth and death rates are:

$$\hat{R}_{b,v,r} = \hat{r}^3 \int_0^{\frac{\hat{r}}{\sqrt[3]{2}}} \frac{\hat{k}_c(\hat{r}', \hat{r}'', \hat{z}, \hat{t})\hat{f}_{v,r}(\hat{r}', \hat{z}, \hat{t})\hat{f}_{v,r}(\hat{r}'', \hat{z}, \hat{t})}{\hat{r}'^3(\hat{r}^3 - \hat{r}'^3)} \frac{\hat{r}^2}{\hat{r}''^2} d\hat{r}' \tag{53}$$

$$\hat{R}_{d,v,r} = \hat{f}_{v,r}(\hat{r}, \hat{z}, \hat{t}) \int_0^1 \hat{k}_c(\hat{r}', \hat{r}'', \hat{z}, \hat{t}) \frac{\hat{f}_{v,r}(\hat{r}', \hat{z}, \hat{t})}{\hat{r}'^3} d\hat{r}' \tag{54}$$

Similarly, the equation for the moving interface turns into the following form.

$$\frac{d\hat{H}_i(\hat{t})}{d\hat{t}} = -\int_0^1 \hat{u}_{ic}(\hat{r}, \hat{t})\hat{f}_{v,r}(\hat{r}, 1, \hat{t}) d\hat{r} \tag{55}$$

Eqs. (52) and (55) should be solved subject to the following boundary and initial conditions:

$$\hat{u}_d(\hat{r},\hat{z},\hat{t})\hat{f}_{v,r}(\hat{r},\hat{z},\hat{t}) - \frac{1}{\hat{H}_i(\hat{t})Pe(\hat{r},\hat{z},\hat{t})}\frac{\partial \hat{f}_{v,r}(\hat{r},\hat{z},\hat{t})}{\partial \hat{z}} = 0 \; at \; \hat{z} = 0, \;\forall\; \hat{t}\,|_{0<\hat{t}\le\infty} \;\&\; \hat{r}\,|_{0\le\hat{r}\le1} \tag{56}$$

$$\hat{u}_d(\hat{r},\hat{z},\hat{t})\hat{f}_{v,r}(\hat{r},\hat{z},\hat{t}) - \frac{1}{\hat{H}_i(\hat{t})Pe(\hat{r},\hat{z},\hat{t})}\frac{\partial \hat{f}_{v,r}(\hat{r},\hat{z},\hat{t})}{\partial \hat{z}} = \hat{u}_{ic}(\hat{r},\hat{t})\hat{f}_{v,r}(\hat{r},\hat{z},\hat{t}) \; at \; \hat{z} = 1, \;\forall\; \hat{t}\,|_{0<\hat{t}\le\infty} \;\&\; \hat{r}\,|_{0\le\hat{r}\le1} \tag{57}$$

$$\hat{f}_{v,r}(\hat{r},\hat{z},\hat{t}) = \hat{f}_{v,r,0}(\hat{r}) \; at \; \hat{t} = 0, \;\forall\; \hat{z}\,|_{0<\hat{z}<1} \;\&\; \hat{r}\,|_{0\le\hat{r}\le1} \tag{58}$$

$$\hat{H}_i(\hat{t}) = 1 \; at \; \hat{t} = 0 \tag{59}$$

In the new dimensionless form, the volume density and dimensionless average droplet size can be calculated as follows.

$$\phi_d(\hat{z},\hat{t}) = \int_0^1 \hat{f}_{v,r}(\hat{r},\hat{z},\hat{t})\,d\hat{r} \tag{60}$$

$$\hat{\mu}_r(\hat{z},\hat{t}) = \frac{1}{\phi_d(\hat{z},\hat{t})}\int_0^1 \hat{r}\hat{f}_{v,r}(\hat{r},\hat{z},\hat{t})\,d\hat{r} \tag{61}$$

3. Numerical analysis

The orthogonal collocation technique (Villadsen and Michelsen, 1978) was used in an element-based form to discretize the internal domain (droplet size). Four and five elements were selected for the non-coalescing and coalescing cases, respectively. The same number of collocation points were adopted for boundary and central elements. The details of the grid generation and the truncation of the internal domain can be found in the supplementary material.

The finite volume method (FVM) with equidistance cells was applied for the spatial direction. MUSCL technique (Anderson et al., 2020) was utilized to discretize the advection terms (including the 1st term at the right-hand side of Eq. (52) that appeared due to the transformation) in order to avoid unphysical oscillatory results due to the strong advection terms. This technique is based on linear profile reconstruction together with slope limiting and subsequent application of the upwind scheme. The described method provides 1st order accuracy for extrema and 2nd order elsewhere. Central differencing was applied to compute the diffusive term. The detail of the FVM technique used is available in the supplementary material.

The discretized governing equation for the dispersion layer (Eq. (52)) by the abovementioned techniques forms a system of ordinary differential equations (ODEs) which were time-integrated together with the transient equation for the moving interface (Eq. (55)). The adaptive Gear's backward differentiation scheme (Gear, 1971) was used to solve the mentioned systems of ODEs.

4. Experimental section

4.1. Chemicals

The following chemicals were used to prepare emulsions: The aqueous phase was composed of 0.1 M of sodium chloride (for analysis, Merck) dissolved in water obtained from a Milli-Q system (Millipore). The model oil phase was prepared by dissolving 800 ppm of Span 80 (Sorbitan monooleate, Fluka) in a solvent composed of 80% wt. Primol 352 (Brenntag Nordic A/S) and 20% wt. decane (Sigma-Aldrich, ReagentPlus ≥99%). The solvent composition was adjusted to obtain viscosity which is high enough to separate the signals for the oil and aqueous phase by NMR. The viscosities and the densities of the oil and aqueous phases are given in Table 1.

4.2. Emulsion preparation

The aqueous phase and then the oil phase (total volume: 30 mL) were introduced into a 60 mL tube. Then the mixture was stirred at 1500 rpm for 3 min using a 4 blades-propeller. Approximately 4.0 mL of the emulsion was then pipetted and introduced into an NMR tube.

4.3. NMR measurements

The measurements were done with a 21 MHz NMR apparatus from Anvendt Teknologi AS (Trondheim, Norway). The sedimentation column was a flat bottom tube with a diameter of 17 mm. The temperature of the sample was maintained at 25 °C by an air-controlled system. The NMR was linked to a PC and controlled via in-house programs developed by Anvendt Teknologi AS. The following physical parameters were obtained:

- Position-dependent water concentration profiles (brine profiles) using a sequence based on previous publications (Hjartnes et al., 2019; Simon et al., 2011; Sjöblom et al., 2021; Sørland, 2014). First the water phase signal was separated from the oil signal using their difference in longitudinal relaxation times (T1). Consequently, a stimulated echo (STE) sequence was applied prior to the profile acquisition, and the z-storage delay in the STE was set to 2.5 s. The profiles were measured every 30 s for 1 h.
- Droplet size distribution (DSD). The sequence starts by only recording the water signal, as explained above. Then, the droplet size distribution is determined by applying the Pulsed Field Gradient (PFG) NMR technique. In this approach, the average surface-to-volume ratio (S/V) of droplets is determined from the apparent restricted diffusion coefficient of water inside droplets measured at a given observation time, while the distribution is assessed from the T2 relaxation time of water as previously described (Sjöblom et al., 2021; Van Der Tuuk Opedal et al., 2009). It must be noticed that Van Der Tuuk Opedal et al. (2009) have compared the DSD distribution obtained by NMR and by another technique (microscopy), and they found a good correlation between the two DSD distributions. However, as the droplets are larger than in previous works (diameter higher than 20 µm), long observation times are required, which may lead to artifacts from the movement of the droplets themselves. Consequently, the average S/V ratio

Table 1 – Viscosity and features of the oil and aqueous phases used to prepare emulsions.

Solvent	Viscosity @ 25 °C (Pa·s) *	Density @ 25 °C (kg/m3) **
NaCl 0.1 M	Not measured	1001.3
Primol 352/decane 80/20 wt%	21.1×10^{-3}	830.9

*: Measured with a Physica MCR 301.
**: Measured with a densitymeter Anton Paar DMA 5000 M.

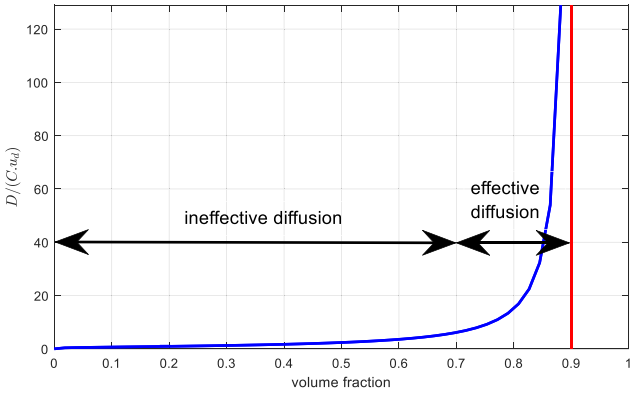

Fig. 2 – Fitted effective diffusion coefficient.

was measured at two different observation times and extrapolated to 0 observation time.

5. Results and discussion

5.1. *Effective diffusion model parameter estimation*

The parameters in the proposed effective diffusion model were estimated by comparing the model predictions with the experimental data for the water in stabilized model oil emulsion described in Section 4. Every experiment (DSD and brine profile measurements) has been performed twice and the results are reproducible. Three initial volume fractions for the emulsions were studied, namely 20%, 40%, and 60%. The model parameters were estimated by simultaneous minimization of the average absolute relative deviation (AARD) for all the data sets as the objective function using MATLAB unconstrained nonlinear optimization functionality (*fminunc*). The deviation was defined as the difference between the measured volume fraction at a spatial location and time, and the model prediction for the whole studied cases. The empirical equation proposed by Kumar and Hartland (Kumar and Hartland, 1985) was used as the slip velocity model (Eq. (29)). This issue is discussed in more detail in Section 5.2. In this study, since the three DSDs depict very similar properties in terms of polydispersity, the maximum volume fraction parameter (ϕ_m) was selected as 0.9, supported by the experimental data. However, as mentioned in Section 2.4, this parameter depends on two main factors, namely, polydispersity (how wide the distribution is and can be expressed by the standard deviation of the DSD) and deformation (which depends on the compressive force in the DPL) and, further modeling of this parameter would be an interesting future study, which might need more experimental cases with more variations in the DSDs. The estimated values for the effective diffusion model parameters are: $C = 5.1 \times 10^{-4} m$, $n = 0.23$, and $m = 1.29$. The volume fraction functionality of effective diffusion coefficient is depicted in Fig. 2.

In Fig. 2, the y-axis shows the relative significance of the diffusion to the advection. Accordingly, we can identify two main regions:

- dispersed phase volume fraction between 0% and 70% with strong advection term and insignificant diffusion term, which can be practically neglected.
- dispersed phase volume fraction between 70% and 90%, in which the diffusion term becomes increasingly more dominant in the governing equation as the volume fraction increases.

As the volume fraction approaches the maximum volume fraction specified in the model (ϕ_m), the diffusion flux asymptotically approaches infinity in the system. The described issue ensures that the dispersed phase volume fraction remains in the physical range (0-ϕ_m). This occurs as the droplets in high-volume fraction regions rapidly diffuse to the surrounding areas with low-volume fractions.

5.2. *Comparison of the slip velocity models*

The three different presented models for the slip velocities in Section 2.3 are compared in Fig. 3 for the case of 40% initial water volume fraction.

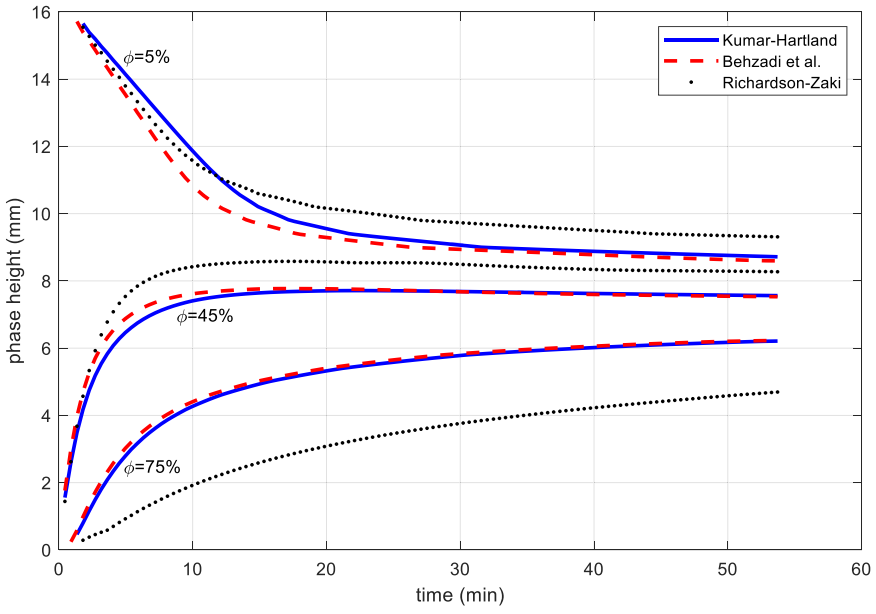

Fig. 3 – Comparison of results of different slip velocity models for water iso-volume fraction curves (initial volume fraction=40%).

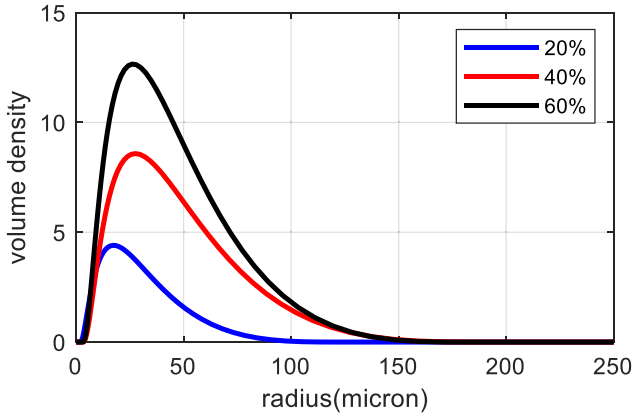

Fig. 4 – Initial DSDs (dimensionless radius-based volume density distribution) for different water volume fractions.

Fig. 3 illustrates the spatial location of iso-volume fractions of 5%, 45%, and 75%. The Kumar and Hartland model (Kumar and Hartland, 1985) and Behzad et al. model (Behzadi et al., 2004) yield relatively matching predictions except for the iso-volume fractions of 5% at the initial time. Nevertheless, the Richardson-Zaki (Richardson and Zaki, 1954) model significantly differs from the other two. Additionally, our attempt to tune the effective diffusivity model parameters while using this slip velocity model could not provide satisfactory results. It is also notable that our result regarding less accurate predictions using the Richardson-Zaki model has also been reported by other researchers (Panjwani et al., 2015). Finally, the Kumar-Hartland model is chosen as the slip velocity model.

5.3. *Comparison of the model and experiment for the non-coalescing system*

This section compares the experimental data to the model predictions for a non-coalescing system with three different volume fractions, 20%, 40%, and 60%. The pertinent droplet size distributions for different initial volume fractions are depicted in Fig. 4. It must be noticed that only minor variations of the DSD could be observed over a period of 45 min after the emulsion preparation which indicates that coalescence is negligible. It must be emphasized again that for all the cases with different initial volume fractions, the same effective diffusion model parameters were used as described in Section 5.1. In Figs. 5–7, the volume fraction profiles and iso-volume fraction curves are shown for various initial volume fractions. The readers can also refer to the supplementary material for a similar comparison using the volume fraction colormaps.

It is worth mentioning that the first 0–1 mm from the bottom of the column is not depicted for the experimental data. It is due to the glass effect that does not allow accurate measurements using the NMR technique for this region.

Overall, good agreement is observed. The main deviation between the experiments and the model results is related to the destabilization period, typically elapsed time between 10 and 20 min when the advection term of the system mainly governs the dynamics. The model does not predict the same level of sharpness for sedimentation fronts. This is more evident in the volume fraction profiles at earlier times and at the top of the column (Figs. 5–7). This deviation can mainly be explained by the fact that the empirical slip velocity models employed are primarily developed based on studying the monodispersed systems. On the contrary, the model provides more accurate predictions for the volume fraction profiles closer to the end of the sedimentation when the advection terms disappear, and the effective diffusion governs the system.

As also mentioned, the same effective diffusion coefficient model was used for all three cases with different initial volume fractions and DSDs. This indicates that the effective diffusion coefficient does not depend strongly on the DSD. Additionally, the effect of physicochemical properties is lumped in the coefficient C in Eq. (31). From the available models for the elastic modulus (to which effective diffusion is directly proportional) for water-oil emulsions (Mason et al., 1997; Mougel et al., 2006; Princen and Kiss, 1986), we expect that the coefficient C is directly proportional to the interfacial tension. Moreover, from the formula for the drag term (to

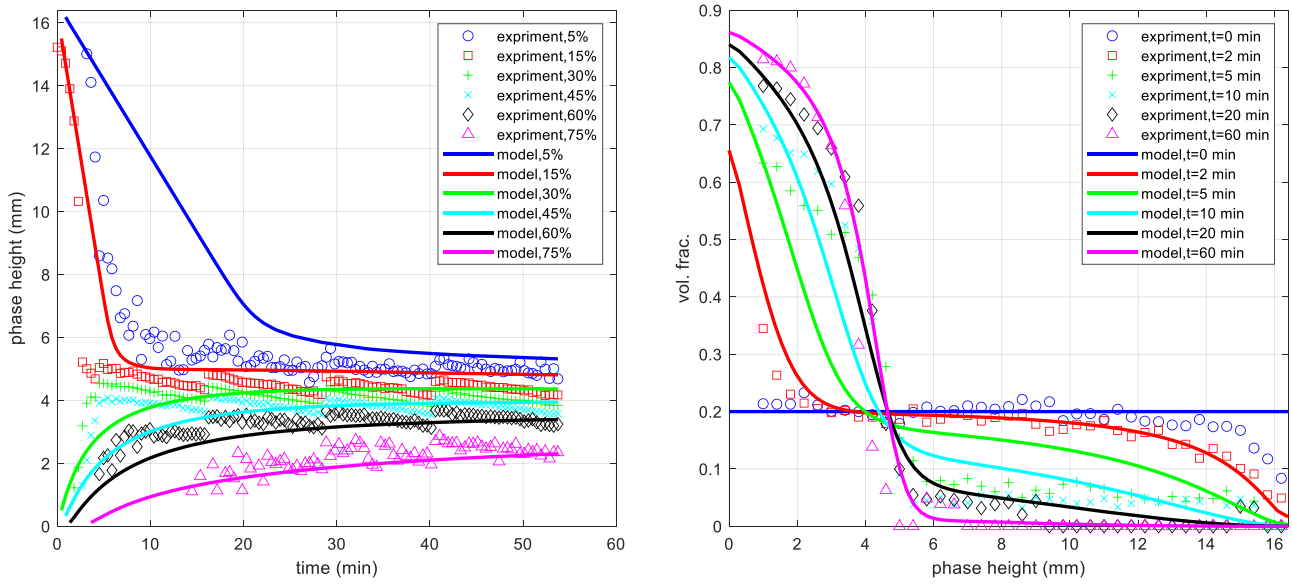

Fig. 5 – Comparison of experiment and model (initial volume fraction=20%), left: various water iso-volume-fraction curves, right: water volume fraction profiles at different elapsed times.

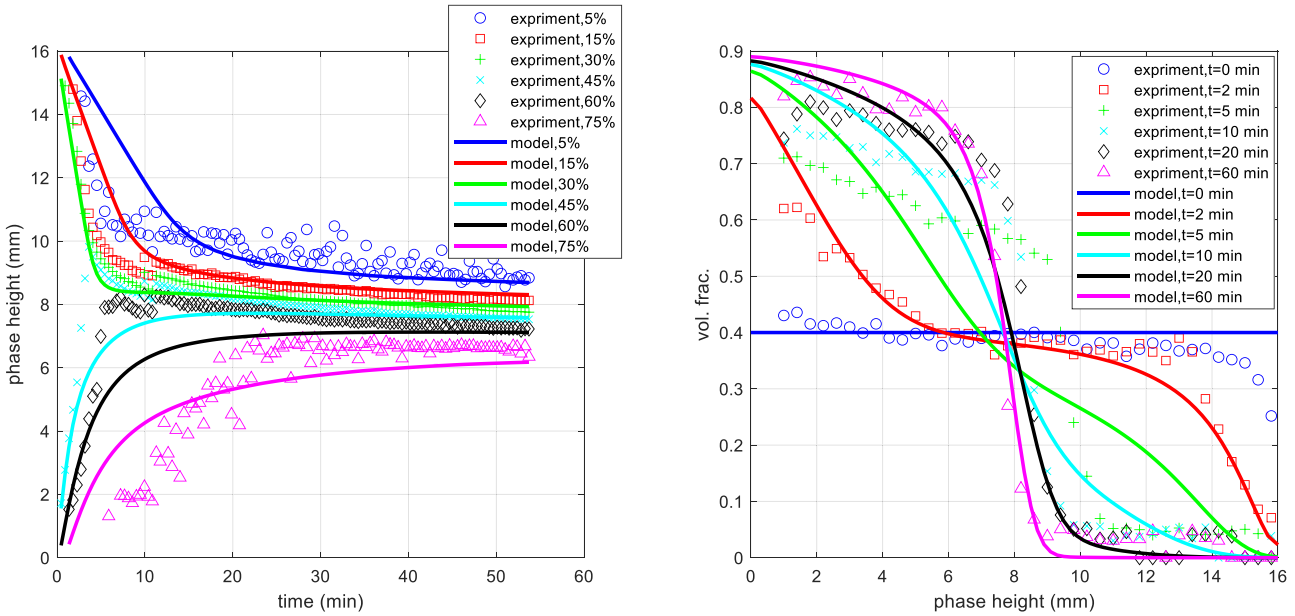

Fig. 6 – Comparison of experiment and model (initial volume fraction=40%), left: various water iso-volume-fraction curves, right: water volume fraction profiles at different elapsed times.

which effective diffusion is inversely proportional) presented by Shih et al. (1986), the C coefficient should also be inversely proportional to the phase density difference and gravitational acceleration. Accordingly, the following proportionality can be deducted for the coefficient C:

$$C \propto \frac{\gamma}{g\,|\rho_d - \rho_c|} \tag{62}$$

Due to measurement range limitation of the tensiometer apparatus (PAT1M from SINTERFACE Technologies), it was not possible to measure interfacial tension value for 800 ppm concentration of Span 80. However, this value should be less than 4.2 mN/m (related to 200 ppm of Span 80 concentration after 1.5 h of adsorption). This limitation did not allow us to corollate the coefficient C according to Eq. (62). However, considering the measurement limitation, we expect a proportionality coefficient less than 203 due to the limitation of the instrument.

5.4. *Case study – a coalescing system*

To evaluate the model results for the system consisting of coalescence, a case study is performed for a water-in-oil system with 40% initial water volume fraction. The model inputs are summarized in Table 2.

The time-space colormaps for volume fraction and the average droplet size are depicted in Fig. 8. At the bottom volume fraction colormap, the formation of the homophase can be observed, which grows at a higher rate until around 3 min; Afterward, it steadily grows at a lower rate. On top of the homophase layer, the formation of the DPL can also be seen. This layer starts to form from the beginning of the

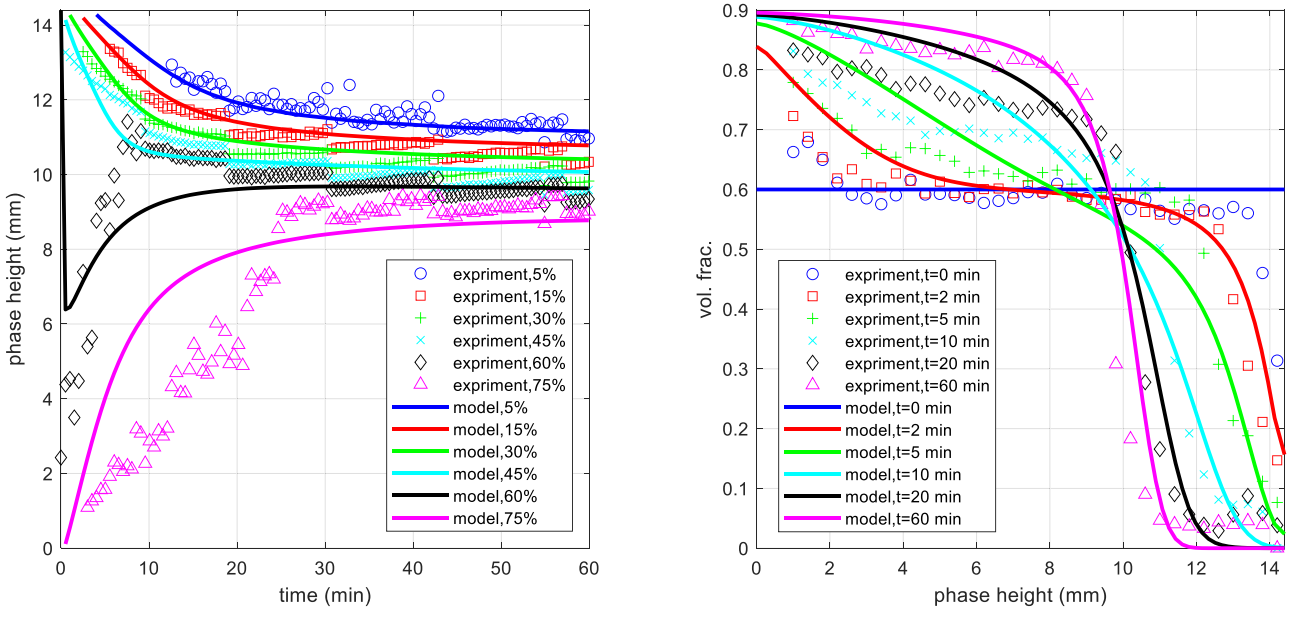

Fig. 7 – Comparison of experiment and model (initial volume fraction=60%), left: various water iso-volume-fraction curves, right: water volume fraction profiles at different elapsed times.

Table 2 – model inputs for the coalescing system case-study.

	Aquous phase	Oil phase
Density (kg/m^3)	1000	850
Viscosity (Pa·s)		20×10^{-3}
Initial vol. Frac.	0.40	
Temperature (K)	300	
Retarded Hamaker constant (N/m^2)	4×10^{-36}	
Interfacial tension (N/m)	15×10^{-3}	
Column height (m)	1.5×10^{-3}	
k_{CR}	1	
k_{CE}	1	
k_{IC}	1	

process; However, the volume friction builds up to the max volume fraction specified for the system, 0.9, at around 4 min. After that, the DPL is fully formed in approximately at a time around 15 min, with its thickness becoming maximum. Then, it shrinks as more water droplets coalesce in the homophase. From the average droplet size colormap for this studied case, the coalescence rate is somewhat faster than the sedimentation rate. As a result, the average droplet size increases from 15 µm to around 40 µm in the first 3 min of the process. Then, due to larger droplet sizes, faster sedimentation rates are observed in the system. Additionally, the increase in the droplet sizes increases the interfacial coalescence time, thus resulting in a slower growth rate of the homophase after 3 min

The volume fraction and average droplet size profiles for different times are shown in Fig. 9. On the right side of Fig. 9, the formation of the homophase can be observed in which the profiles are shifted toward the left. In addition, a drastic increase in both volume fraction and average droplet size can be seen at the bottom of the column as time passes. Here, the volume fraction increases until it reaches a value close to the max volume fraction,0.9. As the volume fraction reaches this point, it remains and does not go higher.

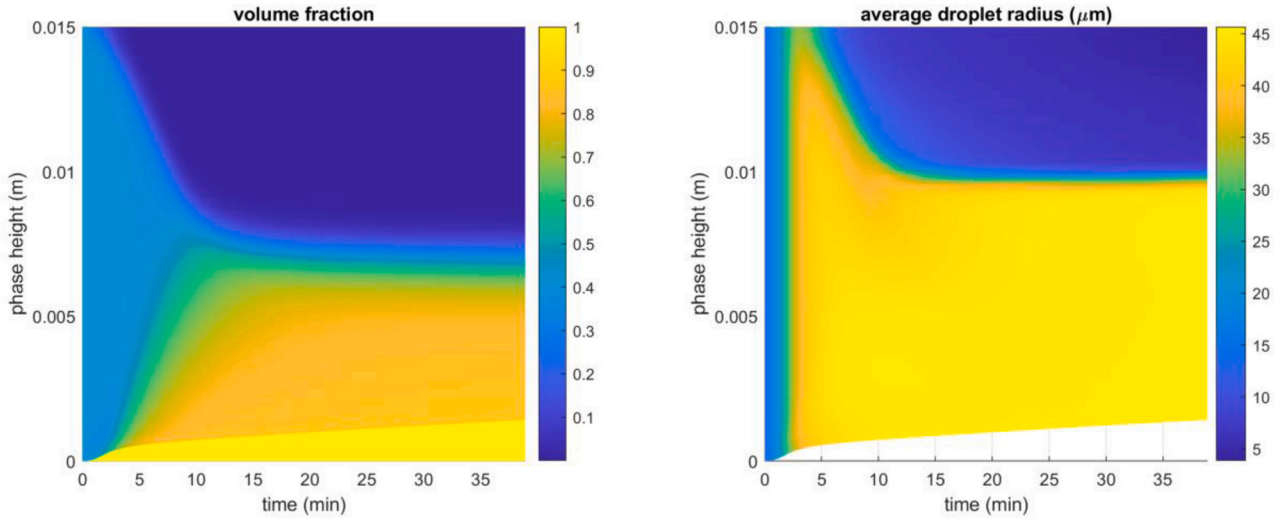

Fig. 8 – Model results colormaps for a coalescing emulsion, initial volume fraction= 40%, right: volume fraction, left: average droplet size.

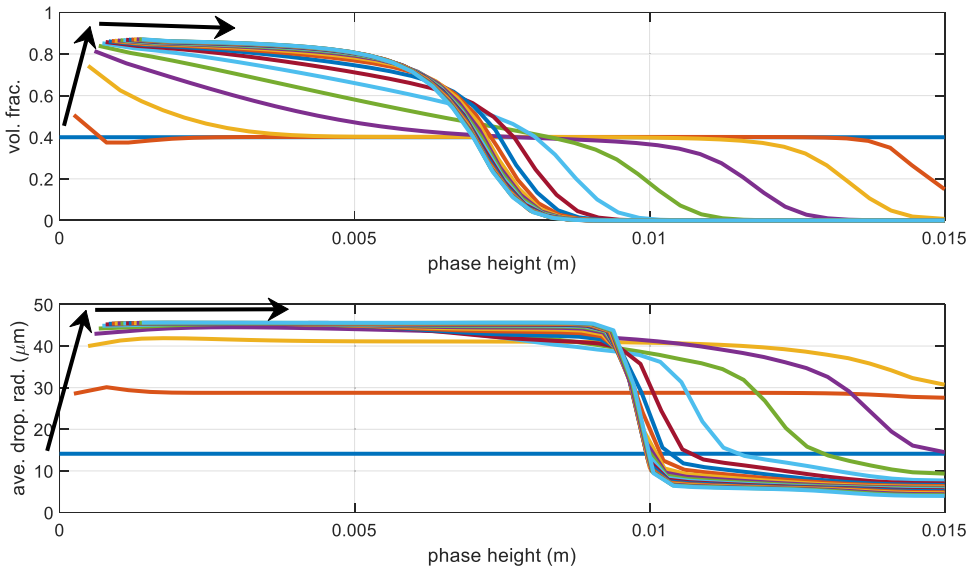

Fig. 9 – Profiles, coalescing emulsion, initial volume fraction= 40%, top: water volume fraction, bottom: average droplet radius.

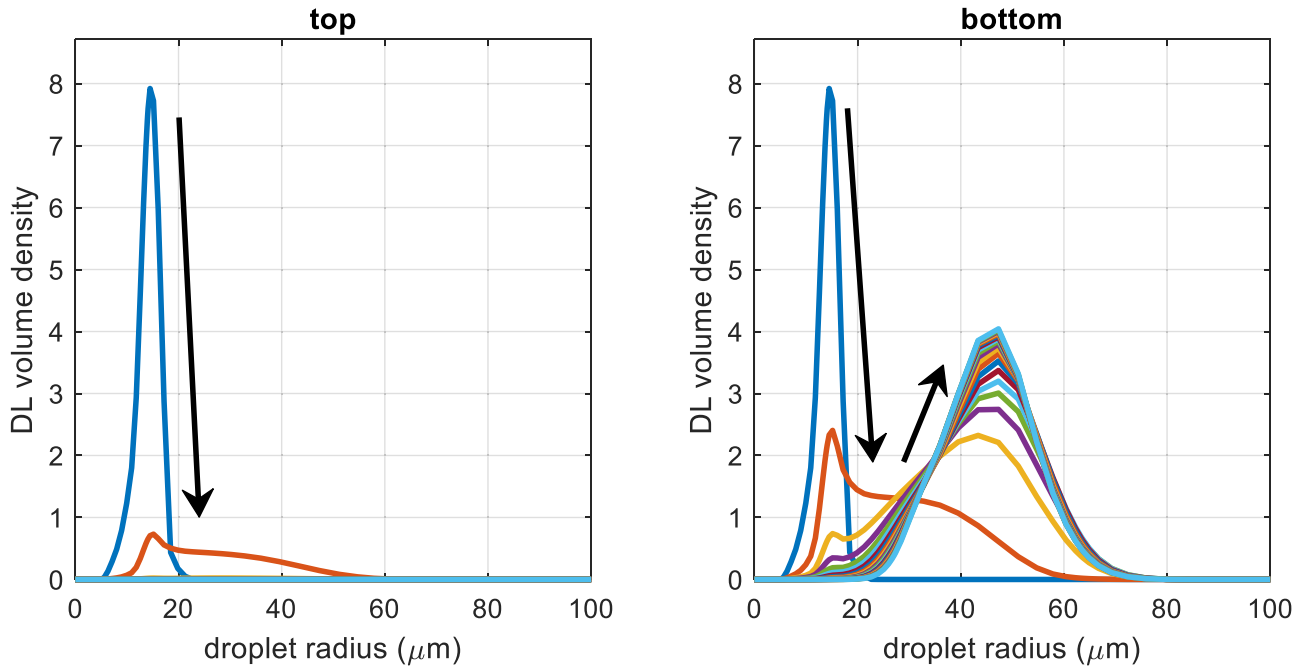

Fig. 10 – Model results for dimensionless volume density distribution, coalescing system, initial volume fraction= 40%, right: top of column, left: bottom of column.

The dimensionless volume density distributions are depicted in Fig. 10 for the top and bottom of the column. At the top of the column, the DSD is rapidly decreasing to zero due to the gravity sedimentation of the droplets to the lower sections of the column. On the contrary, there is a shift toward larger droplet sizes for the bottom of the column. This is a coinciding result of sedimentation and the binary droplet coalescence due to the high-volume fraction in this region.

6. Conclusion

An empirical approach is developed to model the dense-packed layer usually formed in a batch gravity separator. This approach is based on introducing an effective diffusion to the model based on the insight from Shih et al. (1987, 1986). Accordingly, a closure model was proposed for the effective diffusion coefficient with functionalities of the droplet slip velocity and the volume fraction. The selected function for the effective diffusion coefficient asymptotically approaches toward infinity when the volume fraction approaches the maximum allowable volume fraction (as the model parameter). As a result of this high diffusion coefficient, all the excess droplets diffuse back to the surrounding regions with a lower volume fraction. The mentioned issue guarantees that the system's volume fraction is always in the physical range between the zero and maximum allowable volume fraction specified in the model. The described approach was integrated into a general model for the batch gravity separation process. The developed model considers gravity settling/rising of droplets as well as binary and interfacial coalescence using a parallel film drainage model. For slip velocity, three different models were tested and compared and finally, the model by Kumar and Hartland was selected. Furthermore, the model tracks the interface between the dispersion layer and homophase as the homophase grows and the dispersion layer shrinks. This matter results in a moving boundary problem, which was tackled via a spatial-temporal transformation.

Finally, the proposed closure model for the effective diffusion coefficient was tuned using experimental data for a stabilized water in model oil emulsion. Experiments were performed by NMR technique for three volume fractions in the range of 20–60%. The model prediction agrees well with the experiments. Particularly, simultaneous agreement with all cases possessing various initial volume fractions and DSDs suggests that this model can be generalized and applied to a wide range of oil and water emulsions systems. Additionally, the developed model shows promise as it can describe a wide range of initial volume fractions and simultaneously ensure physical values for predicted volume fractions.

For future works we will focus on the below items:

- Applying the model to a coalescing system. That would allow us to tune the interfacial and binary coalescence rates according to a film drainage model with a more realistic assumption by considering the compressive stress force in the DPL as the squeezing force between droplets.
- Comparison between model predictions and experiments for other systems exhibiting different properties. That would allow us to link the effective diffusion coefficient and maximum volume fraction parameter to system physical properties.
- Upscaling of the parameters determined from small-scale experiments.
- Finally, the batch gravity model in this work will be further developed to model the continuous oil/water gravity separators.

Declaration of Competing Interest

The authors declare that they have no known competing financial interests or personal relationships that could have appeared to influence the work reported in this paper.

Acknowledgments

This work was carried out as a part of SFI SUBPRO, a Research-Based Innovation Centre within Subsea Production and Processing. The authors gratefully acknowledge the financial support from SFI SUBPRO, which is financed by the Research Council of Norway (237893), major industry partners, and NTNU. The authors would also like to sincerely acknowledge Total energies Co. for providing the opportunity to use and publish the experimental data.

Appendix A. Supporting information

Supplementary data associated with this article can be found in the online version at doi:10.1016/j.cherd.2023.04.029.

References

Abeynaike, A., Sederman, A.J., Khan, Y., Johns, M.L., Davidson, J.F., Mackley, M.R., 2012. The experimental measurement and modelling of sedimentation and creaming for glycerol/biodiesel droplet dispersions. Chem. Eng. Sci. 79, 125–137. https://doi.org/10.1016/J.CES.2012.05.036

Antonio García, A., Berres, S., Mas-Hernández, E., 2022. A new mathematical model of continuous gravitational separation with coalescence of liquid-liquid emulsions. Chem. Eng. Res. Des. 182, 37–50. https://doi.org/10.1016/J.CHERD.2022.03.044

Antonio García, A., Fernando Betancourt, C., 2019. Conservative mathematical model and numerical simulation of batch gravity settling with coalescence of liquid-liquid dispersions. Chem. Eng. Sci. 207, 1214–1229. https://doi.org/10.1016/J.CES.2019.07.034

Behzadi, A., Issa, R.I., Rusche, H., 2004. Modelling of dispersed bubble and droplet tow at high phase fractions. Chem. Eng. Sci. 59, 759–770. https://doi.org/10.1016/j.ces.2003.11.018

Bury, M., Gerhards, J., Erni, W., Stamm, A., 1995. Application of a new method based on conductivity measurements to determine the creaming stability of o/w emulsions. Int. J. Pharm. 124, 183–194. https://doi.org/10.1016/0378-5173(95)00075-T

Chanamai, R., Herrmann, N., McClements, D.J., 1999. Influence of Thermal Overlap Effects on the Ultrasonic Attenuation Spectra of Polydisperse Oil-in-Water Emulsions. Langmuir 15, 3418–3423. https://doi.org/10.1021/LA981195F

Cunha, R.E.P., Fortuny, M., Dariva, C., Santos, A.F., 2008. Mathematical modeling of the destabilization of crude oil emulsions using population balance equation. Ind. Eng. Chem. Res. 47, 7094–7103. https://doi.org/10.1021/IE800391V/ASSET/IMAGES/LARGE/IE-2008-00391V_0011.JPEG

Anderson, Dale, Tannehill, John C., Pletcher, Richard H., Ramakanth Munipalli, V.S., 2020. Computational Fluid Mechanics and Heat Transfer. CRC Press,.

Deb, T.K., Lebaz, N., Ozdemir, M.S., Govoreanu, R., Mhamdi, A., Sin, G., Sheibat-Othman, N., 2022. Monitoring and Modeling of Creaming in Oil-in-Water Emulsions. Ind. Eng. Chem. Res. 61, 4638–4647. https://doi.org/10.1021/ACS.IECR.1C04722/ASSET/IMAGES/MEDIUM/IE1C04722_0011.GIF

Gear, C.W., 1971. Numerical Initial Value Problems in Ordinary. Differential Equations, 1st ed..,. Prentice Hall,.

Grimes, B.A., 2012, Population Balance Model for Batch Gravity Separation of Crude Oil and Water Emulsions. Part I: Model Formulation. http://dx.doi.org/10.1080/01932691.2011.574946 33, 578–590. https://doi.org/10.1080/01932691.2011.574946.

Grimes, B.A., Dorao, C.A., Opedal, N.V.D.T., Kralova, I., Sørland, G.H., Sjöblom, J., 2012. Separation data. J. Dispers. Sci. Technol. 33, 591–598. https://doi.org/10.1080/01932691.2011.574950

Hjartnes, T.N., Sørland, G.H., Simon, S., Sjöblom, J., 2019. Demulsification of Crude Oil Emulsions Tracked by Pulsed Field Gradient (PFG) Nuclear Magnetic Resonance (NMR). Part I: Chemical Demulsification. Ind. Eng. Chem. Res. 58, 2310–2323. https://doi.org/10.1021/ACS.IECR.8B05165/ASSET/IMAGES/MEDIUM/IE-2018-05165K_M002.GIF

Ishii, M., Zuber, N., 1979. Drag coefficient and relative velocity in bubbly, droplet or particulate flows. AIChE J. 25, 843–855. https://doi.org/10.1002/AIC.690250513

Krieger, I.M., Dougherty, T.J., 1959. A Mechanism for non-Newtonian flow in suspensions of rigid spheres. Trans. Soc. Rheol. 3, 137–148.

Kumar, A., Hartland, S., 1985. Gravity settling in liquid/liquid dispersions. Can. J. Chem. Eng. 63, 368–376. https://doi.org/10.1002/CJCE.5450630303

Mason, T.G., Lacasse, M.D., Grest, G.S., Levine, D., Bibette, J., Weitz, D.A., 1997. Osmotic pressure and viscoelastic shear moduli of concentrated emulsions. Phys. Rev. E 56, 3150. https://doi.org/10.1103/PhysRevE.56.3150

Mills, P., 1985. Non-Newtonian behaviour of flocculated suspensions. J. Phys. Lett. 46, 301–309. https://doi.org/10.1051/JPHYSLET:01985004607030100

Mougel, J., Alvarez, O., Baravian, C., Caton, F., Marchal, P., Stébé, M.J., Choplin, L., 2006. Aging of an unstable w/o gel emulsion with a nonionic surfactant. Rheol. Acta 45, 555–560. https://doi.org/10.1007/S00397-006-0089-Z/FIGURES/5

Oshinowo, L.M., Quintero, C.G., Vilagines, R.D., 2016, CFD and Population Balance Modeling of Crude Oil Emulsions in Batch Gravity Separation—Comparison to Ultrasound Experiments. http://dx.doi.org/10.1080/01932691.2015.1054508 37, 665–675. https://doi.org/10.1080/01932691.2015.1054508.

Oshinowo, L.M., Vilagines, R.D., 2020. Modeling of oil–water separation efficiency in three-phase separators: Effect of emulsion rheology and droplet size distribution. Chem. Eng. Res. Des. 159, 278–290. https://doi.org/10.1016/J.CHERD.2020.02.022

Panjwani, B., Amiri, A., Mo, S., Fossen, M., Linga, H., Pauchard, V., 2015. Dense Packed Layer Modeling in Oil-Water Dispersions: Model Description. Exp. Verif., Code Demonstr. https://doi.org/10.1080/01932691.2014.1003221

Princen, H.M., Kiss, A.D., 1986. Rheology of foams and highly concentrated emulsions: III. Static shear modulus. J. Colloid Interface Sci. 112, 427–437. https://doi.org/10.1016/0021-9797(86)90111-6

Richardson, J.F., Zaki, W.N., 1954. The sedimentation of a suspension of uniform spheres under conditions of viscous flow. Chem. Eng. Sci. 3, 65–73. https://doi.org/10.1016/0009-2509(54)85015-9

Rogers, J.R., Davis, R.H., 1990. Modeling of collision and coalescence of droplets during microgravity processing of Zn-Bi immiscible alloys. 1990. Metall. Trans. A 211 (21), 59–68. https://doi.org/10.1007/BF02656424

Ruiz, M.C., Padilla, R., 1996. Separation of liquid-liquid dispersions in a deep-layer gravity settler: Part II. Mathematical modeling of the settler. Hydrometallurgy 42, 281–291. https://doi.org/10.1016/0304-386X(95)00096-Y

Shih, Y.T., Gidaspow, D., Wasan, D.T., 1987. Hydrodynamics of sedimentation of multisized particles. Powder Technol. 50, 201–215. https://doi.org/10.1016/0032-5910(87)80065-7

Shih, Y.T., Gidaspow, D., Wasan, D.T., 1986. Sedimentation of fine particles in nonaqueous media: Part I — experimental Part II — modeling. Colloids Surf. 21, 393–429. https://doi.org/10.1016/0166-6622(86)80106-8

Shiller, L., Naumann, A., 1935. A Drag Coefficient Correlation. Z. Des. Ver. Dtsch. Ing. 77, 318–320.

Simon, S., Pierrard, X., Sjöblom, J., Sørland, G.H., 2011. Separation profile of model water-in-oil emulsions followed by nuclear magnetic resonance (NMR) measurements: Application range and comparison with a multiple-light scattering based

apparatus. J. Colloid Interface Sci. 356, 352–361. https://doi.org/10.1016/J.JCIS.2011.01.012
Sjöblom, J., Mhatre, S., Simon, S., Skartlien, R., Sørland, G., 2021. Emulsions in external electric fields. Adv. Colloid Interface Sci. 294, 102455. https://doi.org/10.1016/J.CIS.2021.102455
Sørland, G.H., 2014. Dynamic Pulsed-Field-Gradient NMR. Springe Ser. Chem. Phys. 110, i–xiii. https://doi.org/10.1007/978-3-662-44500-6/COVER
Van Der Tuuk Opedal, N., Sørland, G., Sjöblom, J., 2009. Methods for Droplet Size Distribution Determination of Water-in-oil Emulsions using Low-Field NMR The Open-Access Journal for the Basic Principles of Diffusion Theory. Exp. Appl. 9, 1–29.
Villadsen, J., Michelsen, M.L., 1978. Solution of differential equation models by polynomial approximation. Englewood Cliffs, New York. Prentice-Hall,.
Wang, H., Davis, R.H., 1995. Simultaneous sedimentation and coalescence of a dilute dispersion of small drops. J. Fluid Mech. 295, 247–261. https://doi.org/10.1017/S0022112095001959
Zimmels, Y., 1983. Theory of hindered sedimentation of polydisperse mixtures. AIChE J. 29, 669–676. https://doi.org/10.1002/AIC.690290423